Quasiparticle Electronic Structure and Optical Spectra of Single- and Bilayer $PdSe_2$: Proximity and Defect Induced Band Gap Renormalization

Artem V. Kuklin[a,b,*], Hans Ågren[c,d,e]

[a]*Chair of Theoretical Physics and Wave Phenomena, Institute of engineering physics and radio electronics, Siberian Federal University, 79 Svobodny pr., Krasnoyarsk 660041, Russia*

[b]*Department of Chemistry, College of Natural Sciences, Kyungpook National University, 80 Daehakro, Bukgu, Daegu, 41566, South Korea*

[c]*College of Chemistry and Chemical Engineering, Henan University, Kaifeng, Henan 475004 P. R. China*

[d]*Division of Theoretical Chemistry and Biology, School of Engineering Sciences in Chemistry, Biotechnology and Health, KTH Royal Institute of Technology, 10691 Stockholm, Sweden*

[e]*Federal Siberian Research Clinical Centre under FMBA of Russia, Krasnoyarsk, 660037, Russia*

[*]*E-mail: artem.icm@gmail.com*

The fundamental properties of recently synthesized single- and bilayer $PdSe_2$ are investigated using accurate many-body perturbation GW theory to quantitatively examine their electronic structure and explain the insufficiency of previously reported experimental and theoretical results. Including electron-hole interactions responsible for exciton formation, we solve the Bethe-Salpeter equation on top of the GW_0 approximation to predict the optical properties. The fundamental quasiparticle band gaps of single- and bilayer $PdSe_2$ are 2.55 and 1.89 eV respectively. The optical gap of monolayer $PdSe_2$ reduces significantly due to a large excitonic binding energy of 0.65 eV comparable to that of $MoSe_2$, while an increase of the layer number decreases the excitonic binding energy to 0.25 eV in bilayer $PdSe_2$. The giant band gap renormalization of ~36-38% in BL $PdSe_2$/graphene heterostructure has a high impact on the construction of $PdSe_2$-based devices and explains the experimentally observed band gap. The small value of the experimental optical gap of SL $PdSe_2$ (1.3 eV) can be explained by the presence of Se vacancies, which can drop the Tauc-estimated optical gap to ~1.32 eV. The absorption spectra of both mono- and bilayer $PdSe_2$ cover a wide region of photon energy demonstrating promising application in solar cells and detectors. These findings provide a basis for a deeper understanding of the physical properties of $PdSe_2$ and $PdSe_2$-based heterostructures.

KEYWORDS: *first-principles, transition metal dichalcogenide, electron−hole interactions, many-body electronic structure, interface, defects.*

I. INTRODUCTION

During the last decade, great efforts have been made to study two-dimensional transition metal dichalcogenides (TMD) [1–3] which belong to a special class of materials with a wide variety of technologically useful properties. For example, single-layer (SL) MoS_2 demonstrates indirect-direct bandgap transitions with the decrease in the number of layers [4] indicating a great potential of optoelectronic applications [5–8]. TMDs are considered as two-dimensional electronics materials that can be more flexible than graphene in the prospect of nanoelectronic applications because the former ones have a variable band gap. By changing the number of layers, one can modify physical parameters like optical transitions, conductivity, electron mobility, electronic relaxation [9,10].

Noble-metal dichalcogenides attract special attention due to their atomic and electronic properties [11–16]. Recently, the first air-stable monolayer (ML) of a dichalcogenide has been exfoliated from a bulk crystal of $PdSe_2$ [15] showing an intriguing pentagonal morphology. In contrast to rapidly degradable black phosphorus, $PdSe_2$ is highly stable under ambient conditions enabling the possibility to utilize it as a field-effect transistor [17], thermoelectric material [13,18], and catalyst for water splitting [19]. The growth of bilayer (BL) $PdSe_2$ on graphene was carried out by molecular beam epitaxy (MBE) demonstrating flexible nanoscale electronic junctions [20]. However, despite a few reported theoretical and experimental investigations of single- and bilayer $PdSe_2$, their electronic and optical properties have remained unsettled. For instance, the band gap of epitaxial bilayer $PdSe_2$ has been measured by scanning tunneling spectroscopy (STS) technique on the top of graphene and bigraphene [20]. However such kind of heterostructures are expected to result in band gap renormalization [21] caused by proximity induced interlayer interaction. At the same time, optical gaps of mechanically exfoliated $PdSe_2$ layers [15] was likely affected by defects which play a major role in electronic and sometimes in geometrical properties of semiconductors [22]. It is a common fact that point defects occur during exfoliation and growth of monolayers. Usually, TMD is prone to form chalcogen vacancies [23–26], which result in deep in-gap states [27–29] or substitutional formation of single-atom oxygen sites [30,31]. Due to the structural features of $PdSe_2$ and relatively high exfoliation energy, it is expectedly more sensitive to defect formation than Mo dichalcogenides. Like other 2D dichalcogenides [32–34]. $PdSe_2$ is expected to demonstrate large excitonic effects, which will decrease its fundamental band gap and affect the optical properties. Therefore, it is of high importance to quantitatively explore basic properties of SL and BL $PdSe_2$, which have not been reported previously and explain insufficiency

of previously reported experimental and theoretical results. Thus, it is essential to accurately predict the band structure and optical response of these materials using an accurate many-body approach.

In this paper we use for the purpose the quasiparticle (QP) GW [35,36] method with the subsequent solution of the Bethe-Salpeter equation (BSE) including electron-hole interactions [37–39] applied on mono- and bilayer $PdSe_2$. First, we discuss structural and electronic properties calculated within optPBE and the screened exchange hybrid density functional proposed by Heyd-Scuseria-Ernzerhof (HSE06) [40] implemented in the VASP code [41,42] to analyze the main structural features of SL $PdSe_2$. This is followed by quasiparticle band structure calculations to get accurate band gap values. Next the renormalization of the bilayer $PdSe_2$ band gap caused by interaction with graphene is calculated to explain the failure of reported disagreement between current-voltage (dI/dV) experimental data and PBE data. A well-converged dielectric function and optical spectra are calculated taking into account the excitonic effect within the BSE approximation. At the final step, the theoretical and experimental optical gaps of SL $PdSe_2$ are compared and explained.

II. COMPUTATIONAL METODS

First-principles calculations were performed within the framework of van-der-Waals density functional theory (vdW-DFT) with a plane-wave basis set as implemented in the Vienna Ab initio Simulation Package (VASP) [41,42]. The projector augmented wave (PAW) [43] method and optimized Perdew-Burke-Ernzerhof (optPBE) [44] exchange functionals were employed. The exchange hybrid density functional proposed by Heyd-Scuseria-Ernzerhof (HSE06) [40] was also used. Sixteen valence electrons were included in Pd pseudopotential. The quasiparticle band structures were calculated using the many-body GW method [35,36] with both single-shot G_0W_0 and iterative GW_0. Wannier interpolation procedure performed in the WANNIER90 code [45] was used to plot GW band structures on a fine k-path contained 60 points in each direction. The Bethe-Salpeter equation in the Tamm-Dancoff approximation [37–39], using eight highest valence bands and eight lowest conduction bands, was employed to correctly account for the electron-hole interaction necessary to obtain accurate excitonic spectra. Calculations of the dielectric tensor within the BSE approach were performed starting from the GW_0 wave functions and eigenvalues while using optPBE orbital derivatives. The dielectric matrix was output on a fine energy grid of 667 points/eV. The first Brillouin-zone (BZ) for periodic optPBE and HSE calculations was sampled on a gamma-centered grid of $12\times12\times1$ k-points according to the Monkhorst-Pack scheme [46],

while the well-converged 8×8×1 *k*-grid used for GW and BSE calculations. The cutoff energy for the plane wave expansion of the wave functions was set to 400 eV. The number of conduction bands used in the calculations was increased ~4 times with respect to the occupied bands. We carefully tested this number and found that an increase in 20 times does not significantly affected the band gap (~0.05 eV). It was shown that limited number of conduction bands can affect the eigenvalues of hexagonal BZ [33], however, the present monoclinic cell converges much faster. The energy cutoff of 270 eV for the G vector was chosen. The convergence tolerances of the force and electronic minimizations were 10^{-3} eV/Å and 10^{-5} eV, respectively. A vacuum region of >15 Å was set to avoid artificial interaction between neighboring images and correctly calculate optical properties. The interface of BL $PdSe_2$ and graphene was matched and created using the Virtual NanoLab (VNL) tool [47,48]. The Visualization for Electronic and Structural Analysis software (VESTA) [49] were used for the results visualization.

Due to the possible coexistence of two phases of bulk $PdSe_2$ at certain conditions, [50] to describe accurately its geometry and electronic structure we first tested several density functional theory (DFT) functionals including PBE [51] with and without DFT-D2 and DFT-D3 corrections of Grimme [52,53], optPBE, vdW-DF, vdW-DF2, optB86b-vdW, and optB88-vdW [44]. The optPBE functional demonstrates reasonable results for both structural and electronic properties. General trend corresponds to results of Oyedele A.D. et al. [15]. The structural parameters of *a*=5.87, *b*=5.99 and *c*=7.90 Å are in agreement with experimental data (*a*=5.75, *b*=5.87 and *c*=7.69 Å) [50]. Some functionals like PBE DFT-D2 and DFT-D3 yield a barrier-free transformation into pyrite-like structures, where *c* direction is decreased with following interlayer coupling of Pd and Se atoms. The increase in basis set gives qualitatively similar results. Due to the failure of some functionals to calculate the correct phase of $PdSe_2$, it is highly important to choose a proper functional for further theoretical calculations. Further, the optPBE functional is used to find $PdSe_2$ equilibrium geometry.

III. RESULTS AND DISCUSSION

The single-layer $PdSe_2$ is obtained by cutting off one stoichiometric layer from bulk $PdSe_2$, which crystallizes into an orthorhombic PdS_2-type structure with the *Pbca* space group of symmetry at ambient conditions [54]. Each Pd atom is four-coordinated to a selenium atom (Fig. 1(a)). This is the result of the d^8 state of typical Pd^{2+} complexes, which prefers to adopt square-planar coordination. The relaxed single layer $PdSe_2$ lowers the symmetry to the $P2_1/c$ space group with structural parameters of *a*=5.72, *b*=5.93 Å, and β=87.6°, which are in good agreement with

previously reported theoretical [55] and experimental data [15,17]. The calculated total energy of the monolayer is 412 meV per formula unit is higher than that of bulk $PdSe_2$ and corresponds to the previously reported energy range (280-570 meV/$PdSe_2$) [13].

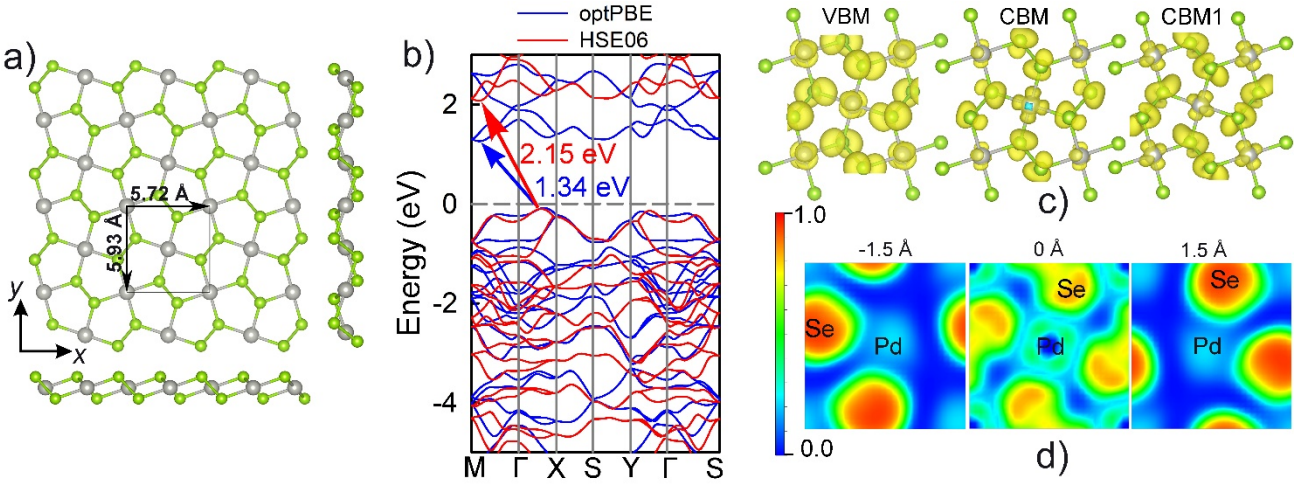

FIG. 1. (a) The top and side views of single-layer $PdSe_2$. The yellow and gray atoms represent Se and Pd respectively. (b) The band structure of single-layer $PdSe_2$ calculated within optPBE (blue) and HSE06 (red) levels of theory. The Fermi level is set to 0 eV. (c) Spatial distribution of electron density in VBM (left panel, 0.0002 e/Å^3), CBM and CBM1 (middle and right panels, 0.005 e/Å^3) states. (d) The electron localization function of monolayer $PdSe_2$ renormalized between 0.0 and 1.0. Delocalized and localized electrons are represented by values of 0.5 and 1.0, respectively.

The lowering of symmetry is caused by breaking of interlayer coupling between the $4d_z^2$ orbitals of Pd in one layer and the $4p_z/3d_z^2$ orbitals of Se in the next layer, which is clearly seen from the deformation of the band structure plotted in Fig. S1. Weak overlap is responsible for micromechanical cleavage and prevents transformation to the pyrite-type structure. By fixing lattice constants of the monolayer to the bulk values, the bands responsible for $4p_z$ and $3d_z^2$ orbitals of Se in the high-energy region are systematically lowered by several meV. Loss of the neighbor layers results in relaxation of the cell shape.

The electronic band structure of SL $PdSe_2$ in Fig. 1(b) exhibits an 1.34 eV indirect band gap calculated at the optPBE level of theory that agrees well with previously reported data (1.45 and 1.30 eV calculated at PBE and optPBE levels) [13,15]. Taking into account long-range correction at the HSE06 level, the band gap is increased up to 2.15 eV. The previously reported HSE06 band gaps are 2.22 and 2.28 eV [19,56]. The valence band maximum (VBM) and conduction band minimum (CBM) are located between the high symmetrical points: Γ-X and M-Γ, respectively. Figure 1(c) demonstrates the spatial distribution of electron density in VBM and CBM. The shape of electron density refers to the main contribution from Se $4p_z$ and Pd $4d_z^2$ orbitals in VBM whereas CBM is

represented by Pd in-plane orbitals. Bonding in solids can be classified by electron localization function (ELF). The ELF of monolayer $PdSe_2$ renormalized in the values between 0.0 and 1.0 is shown in Fig. 1(d), where delocalized and localized electrons are represented by values of 0.5 and 1.0, respectively. The clear overlap between in-plane Pd 4*d* and Se 4*p* states results in covalent bonding in the monolayer, which is similar to other TMDCs. However, the bonding is not strong, but rather soft, which is confirmed from reported elastic constants of Pd chalcogenides [57]. The electronic structure of bilayer $PdSe_2$ demonstrates a similar dispersion of VBM and CBM states decreasing the band gap to 0.81 (optPBE) and 1.62 eV at the HSE06 level (Fig. S2, Table I). Therefore, the use of HSE06 functional greatly enhances the band gap width of both SL and BL $PdSe_2$.

As the experimentally measured band gaps of SL and BL $PdSe_2$ are 1.30 and 1.15±0.07 eV respectively [15,20], it seems that optPBE functional works quite well. However, comparison of experimental measurements to PBE level data cannot guarantee the correctness of reported band gaps, while state-of-art GW and BSE levels of theory makes it possible accurately predict the fundamental and optical energy gaps taking into account many-body effects including electron-electron and electron-hole interactions. The quasiparticle G_0W_0 and GW_0 band structures of ML and BL $PdSe_2$ are plotted in Fig. 2 after the Wannier interpolation procedure performed in the WANNIER90 code [45]. The quasiparticle eigenvalues are interpolated on a finer k mesh of 360 points. Generally, the form of QP bands agrees well with those calculated at the optPBE and HSE levels (Fig. 1(b)). The materials demonstrate indirect band gaps within the M-X region with values of 2.55 and 1.89 eV at the GW_0 level for ML and BL, respectively, that is quite close to G_0W_0 (2.53 and 1.79 eV, respectively) (Table I). This small disagreement of G_0W_0 and GW_0 in bilayer $PdSe_2$ band alignment likely results from the screening part of the iterative wave function in the GW_0 approach, which makes it possible to take into account weak interactions between layers at the more precise level compared to the noniterative G_0W_0 approach. Note that the slope of CBM in bilayer $PdSe_2$ becomes steeper due to interlayer interactions that involve $4p_z$ Se orbitals contributing to CBM. The self-consistent GW_0 approach, in which the Green function (G) is iterated while keeping the screened interaction (W) fixed during an iteration of the Dyson equation, generally demonstrates a more accurate prediction of band gaps [58].

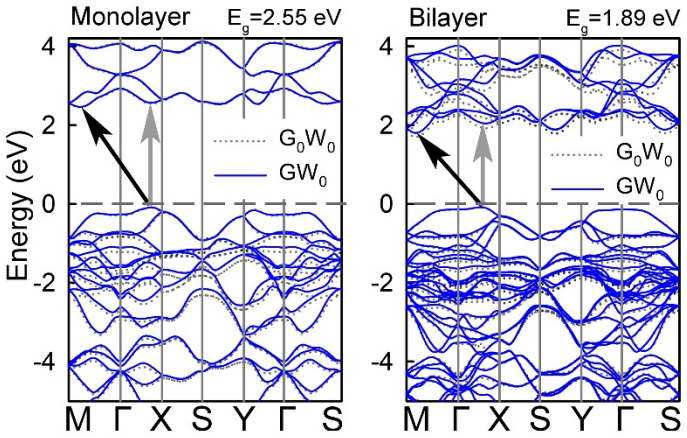

FIG. 2. Quasiparticle G_0W_0 (dotted black) and GW_0 (solid blue) band structures of single-layer (left) and bilayer (right) $PdSe_2$. The black and grey arrows correspond to indirect and direct band gaps. (b) Partial DOS of BL $PdSe_2$/graphene calculated within optPBE functional. The Fermi level is set to 0 eV.

Table I. Comparison of $PdSe_2$ band gaps (eV) obtained with various methods.

		Single-layer	Bilayer
present work	optPBE	1.34	0.81
	HSE06	2.15	1.62
	G_0W_0	2.53	1.79
	GW_0	2.55	1.89
	optical gap	2.01	1.89
reported	optPBE	1.34[a]	0.81[a]
	PBE	1.3[a]	0.92[a]
		1.43[b]	0.94[c]
	HSE	2.22[d]	-
		2.28[e]	
Exp. optical gap (Tauc plot fitting)[a]		1.30	1.0
Exp. gap (on the top of graphene)[c]		-	1.15 ± 0.07

[a, b, c, d, e] References [15], [13], [20], [19], [61] respectively

The calculated quasi-particle band gaps are much larger than those found experimentally. First, for preserving the order of the narrative, we give reason for the experimental band gap of bilayer $PdSe_2$ being 1.15±0.07 eV [20]. For a quantitative comparison of BL $PdSe_2$ between reported experimental data and theory, we have to take into account the graphene substrate that is interacting with BL $PdSe_2$ and expected to affect its the energy gap. The large supercell containing 76 atoms in total is constructed to avoid any mismatch-induced effects (Fig. 3(a)). To reduce the high computational cost of accurate electronic structure calculations, the projected density of states (PDOS) of BL $PdSe_2$ on the top of graphene is calculated using the optPBE functional (Fig. 3(b)) with following band gap reevaluation at the HSE06 level. It is important to note that the relative shape and the Fermi level position of the calculated DOS correspond to that reported within experimental STS measurements. Though the optPBE method cannot correctly reproduce the band gap width, we can expect a very good quantitative correlation in the percentage of its decrease.

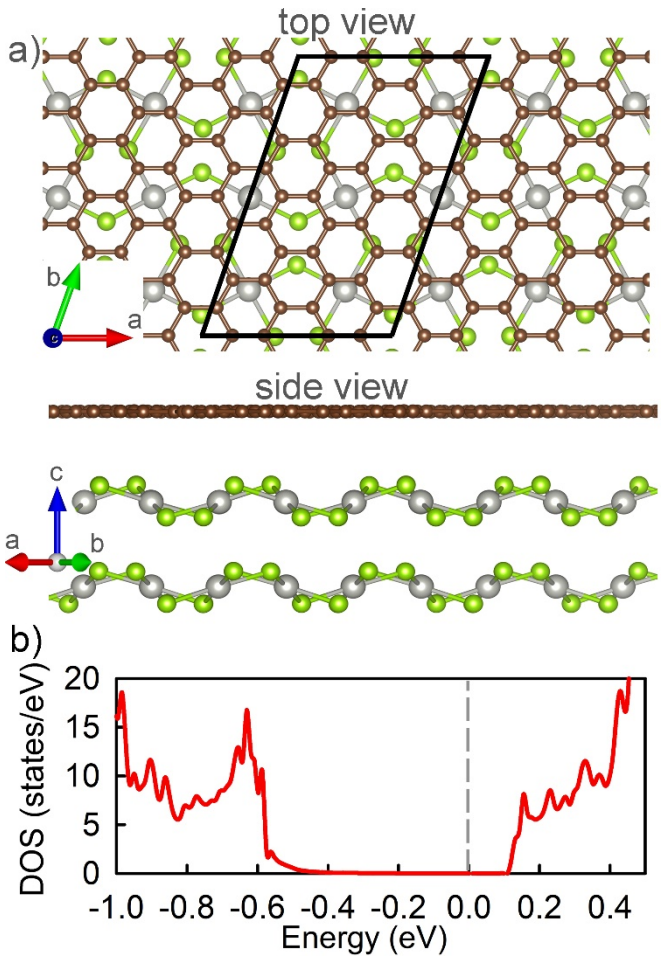

FIG. 3. (a) The equilibrium geometry of simulated heterostructure and (b) partial DOS of BL $PdSe_2$/graphene calculated within optPBE functional. The Fermi level is set to 0 eV.

In Fig. 3(b) one can observe the BL $PdSe_2$ renormalized band gap of 0.51 eV, which is ~38% reduction in comparison to that of freestanding BL $PdSe_2$. The HSE06 level demonstrates a 36% decrease of the band gap. Therefore taking into account the percentage of decrease, a renormalization at the QPGW level should lead to the band gap of 1.19±0.02 eV that is in excellent agreement to the reported one (1.15±0.07 eV) [20]. This means that the satisfactory agreement of previously reported PBE values is just accidental and it should be modified with respect to the BL $PdSe_2$/graphene interaction.

Next, we consider the optical properties of $PdSe_2$ (Fig. 4). In order to include electron-hole interactions responsible for exciton formation, we solve the Bethe-Salpeter equation on top of the GW_0 approximation. BSE spectra are obtained in the Tamm-Dancoff approximation by using the eight highest valence bands and eight lowest conduction bands. To check the convergence we increase the number of conduction bands by 50% and find that the difference in the first transition peak is equal to 0.001 eV which is much smaller than the accuracy of the experimental method. We perform the convergence procedure of the band gap width and the first exciton peak position versus a number of k-points at the G_0W_0 level because it demonstrates very close results to that of GW_0 (Fig. 2) while it is far less time-consuming. At a chosen 8×8×1 *k*-grid, the quasiparticle gap is converged within 0.05 eV (Fig. 4(a)) while the first peak in the imaginary part of the dielectric function is converged within 0.01 eV. The BSE calculations show that even a 6×6×1 k-grid can produce a qualitatively good dielectric function comparable to that of the 14×14×1 grid (Fig. 4(a)) whereas qualitatively erroneous result is however observed when the k-grid is decreased to 4×4×1, where the amplitude of peaks becomes significantly different. The dielectric function is evaluated at the grid of 667 points/eV. The indirect transitions are not included because they require an account of nontrivial exciton-phonon interactions and least probable. Thus, only direct optical transitions like that shown schematically in Fig. 4(b) are included. In the experimental characterization, the single-layer $PdSe_2$ was placed on the top of 280 nm SiO_2 slab, which possesses low polarizability. Therefore, band gap renormalization by interaction with the SiO_2 layer (as we discuss above in BL $PdSe_2$/graphene) is least likely and can be neglected.

In the infrared region, absorption approaches zero and $PdSe_2$ becomes transparent. In the visible region, absorption gets stronger and shows an exponential dependence until ~2 eV in SL and ~1.9 eV in BL $PdSe_2$. In single-layer $PdSe_2$ the dependency of the dielectric function on the polarization axis is stronger than that of the bilayer. The first optical transition (A exciton) in monolayer $PdSe_2$ occurs at the photon energy of 2.01 eV (Fig. 4(c)) corresponding to its optical

band gap, which is 0.54 eV narrower than the fundamental indirect band gap (Table I). The second peak in the (yy) imaginary part of the dielectric function occurs at 2.48 eV. However, there exists one more prominent peak of (xx) ε_2 part at 2.19 eV between those of (yy) direction. The optical gap in bilayer $PdSe_2$ is equal to 1.89 eV (Fig. 3(d)) and is the same as the fundamental indirect energy gap. It can be noted that the band gaps found within the HSE06 functional approach are close to the optical gaps and thus it can be used for the purpose to give a first estimation of E_{opt_g}.

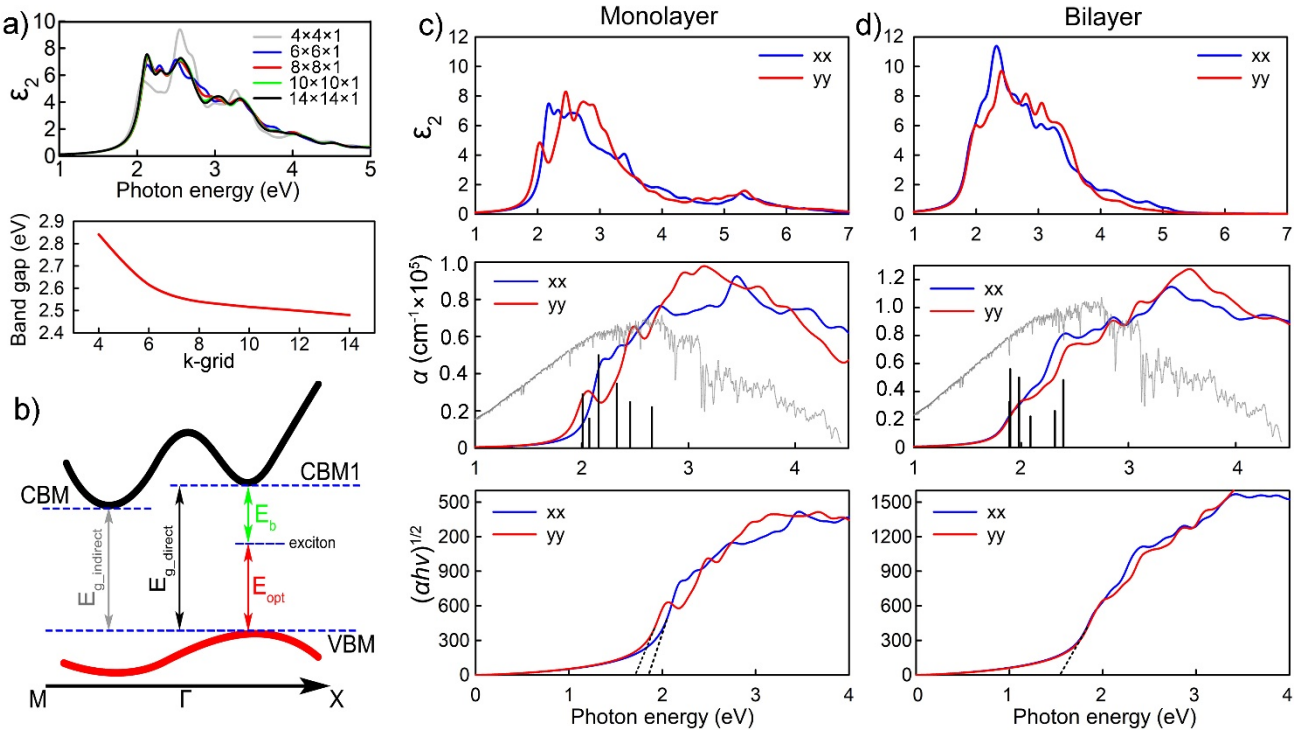

FIG. 4. (a) Convergence of the imaginary part of the dielectric function (top) and the QP band gap (bottom). (b) Schematic illustration of an optical transition. (c,d) Optical properties of ML and BL $PdSe_2$: imaginary part of dielectric function (top panels); absorption coefficient (middle panels), the most prominent oscillator strengths are plotted by black bars, the grey line corresponding to the incident AM1.5G solar flux is given for view; Tauc plots (bottom panels), the dashed lines are linear fitting the curves.

A large exciton binding energy of 0.65 eV corresponding to the energy difference in the fundamental direct band gap and first optical transition in the monolayer is observed for the lowest energy exciton. The found excitonic effect has actually the same value as for the $MoSe_2$ monolayer (0.65 eV) [21]. Increasing the number of layers to the bilayered structure significantly reduces exciton binding energy to 0.25 eV while giving rise of a little bit weaker bound excitons. The peak positions in BL $PdSe_2$ are slightly shifted in comparison to that of isolated SL $PdSe_2$ resulting from a shift of band positions. The distinctive peak at ~1.8 eV, which is not included in Fig. 4(d) due to its small oscillator strength (~0.001% of intralayer exciton peak), appears in the absorption spectrum of

BL $PdSe_2$. This feature might correspond to interlayer excitations, which result from electrons and holes of different monolayers. However, the probability of their formation is too low to consider them for practical formation of the confined exciton condensate [59,60].

The first excitonic peaks involve Pd dxy/dz^2 and Se pz orbitals, which are responsible for interband transitions. At higher energies, between 2.7 and 4.0 eV, the absorption processes reach maximum, accumulating a major part of light in the violet and ultraviolet regions. The main absorption peak of ML occurs at 3.15 eV. This value is in good agreement with the reported experimental absorbance spectra where a peak locates at ~3.17 eV [15]. The main peak shifts to the ultraviolet region in the theoretical spectrum of bilayer $PdSe_2$ and locates at 3.56 eV. In comparison to silicon, which is widely used for single-crystalline thin film solar cells [38], the imaginary parts of the $PdSe_2$ dielectric functions (Figs. 4(c,d)) cover a wider visible spectrum, something that should be reflected in a much higher efficiency of sunlight harvesting. We expect that mono- and bilayer $PdSe_2$ can capture a significant fraction of sunlight in the visible and ultraviolet regions, and can thus be used for construction of solar panels on a spacecraft. Moreover, the proposed combination of $PdSe_2$ thin films with Si substrates makes it possible to construct highly sensitive fast photodetectors [61].

The experimental band gap of monolayer $PdSe_2$ was obtained from the optical absorption spectra through linear extrapolation of a Tauc plot [15]. A band gap can be extracted from the linearity of the plots of $(\alpha h\nu)^{1/n}$ versus photon energy, where α is the absorption coefficient, h is Plancks constant, ν is photon energy, and n for allowed transitions is either 1/2 or 2 for direct and indirect band gap, respectively. Here, we use n=2, because $PdSe_2$ is an indirect semiconductor. The linear extrapolation of $(\alpha h\nu)^{1/2}$ in Fig. 3(c) gives a band gap of 1.71 eV, which is still larger than that of 1.3 eV obtained experimentally [15] and smaller than the optical gap calculated within BSE (2.01 eV). The Tauc plot of bilayer $PdSe_2$ is given in Fig. 4(d) as a guide for future experiments (the gap is 1.55 eV).

The possible presence of defects could drop the band gap width. The most important factor in defect formation is the significantly strong $PdSe_2$ interlayer binding energy, which can lead to the appearance of a high amount of Se defects caused by mechanical exfoliation. The defects can be represented by vacancies or by adatoms. On the one hand, a calculation at the optPBE level electronic structures of monolayer $PdSe_2$ with introduced Se vacancies reveal a decrease of the band gap down to half the value depending on the number of vacancies. For example, monolayer Pd_8Se_{15} (i.e. one vacancy per four unit cells) is characterized by an energy gap of 0.67 eV whereas

monolayer $Pd_{32}Se_{63}$ (i.e. one vacancy per sixteen unit cells) demonstrates a gap of 1.03 eV which represents a 23% decrease (Fig. 5, red line). As can be seen, even a low concentration of Se vacancies can introduce in-gap states reducing the band gap. After renormalization of the Tauc-estimated band gap, a gap of 1.32 eV is predicted, which is close to the reported experimental value (1.3 eV). It should also be noted that an Se-deficient condition in the bulk phase could lead to a decrease of the interlayer distance with a subsequent chemical transformation to Pd_2Se_3 [16]. On the other hand, Se adatoms ($Pd_{32}Se_{65}$) can be effectively absorbed by the $PdSe_2$ monolayer embedding into the mother structure with zero energy cost (Fig. S3). Likely, future experiments on modification of single-layer $PdSe_2$ by Se adatoms will make it possible to discover a new phase or new monolayer in the Pd-Se system. Note here that adatoms do not decrease drastically the band gap (1.24 eV or 7.5%) (Fig. 5, blue line).

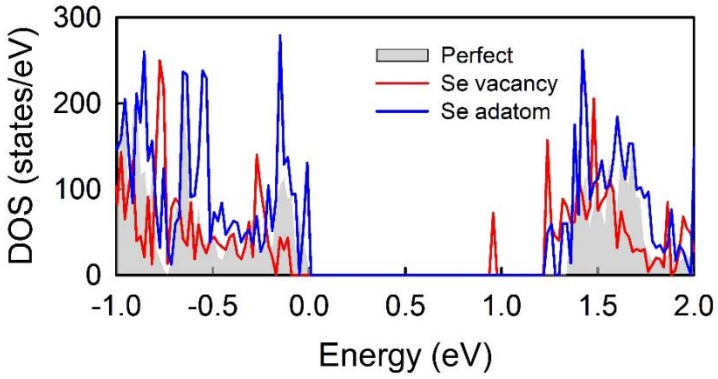

FIG. 5. The comparative DOS of perfect and defective monolayer $PdSe_2$

Hence, the fundamental band gap in defect-free single-layer $PdSe_2$ is 2.55 eV and it decreases to the optical gap of 2.01 eV by the presence of a large exciton binding energy. The previously found significantly small value of the experimental optical gap of SL $PdSe_2$ can be explained by the presence of Se vacancies, which can drop the Tauc-estimated band gap width to ~1.3 eV.

IV. CONCLUSIONS

We have carried out first-principles GW-BSE calculations to study the electronic properties and optical spectra of single- and bilayer $PdSe_2$ including many-body effects. The materials are indirect band gap semiconductors with gap values of 2.55 and 1.89 eV for the monolayer and bilayer, respectively. The monolayer $PdSe_2$ demonstrates a large exciton binding energy of 0.65 eV for the lowest energy exciton (2.01 eV) comparable to that of single layer $MoSe_2$. The inconsistency

of band gaps in the reported experimental and theoretical data is interpreted by giant band gap renormalization in the BL $PdSe_2$/graphene heterostructures and the presence of defect-induced embedded states in the monolayer $PdSe_2$ band gap. These findings explain the reason for the experimentally observed band gaps. The optical spectra of $PdSe_2$ reveal a possible highly efficient sunlight absorption in a wide region of photon energy and could have a high impact on further applications of $PdSe_2$ based materials.

ACKNOWLEDGMENTS

This work is supported by the government contract of the Ministry of Education and Science of the Russian Federation to Siberian Federal University (Grant No. 16.1455.2017/PCh). H.Å. acknowledges the support of the Russian Science Foundation (Project No. 18-13-00363). The authors thanks the Irkutsk Supercomputer Center of SB RAS for providing access to HPC-cluster "Akademik V.M. Matrosov" and Prof. Pavel V. Avramov at the Kyungpook National University for fruitful discussions.

References

[1] S. Manzeli, D. Ovchinnikov, D. Pasquier, O. V. Yazyev, and A. Kis, Nat. Rev. Mater. **2**, 17033 (2017).

[2] W. Choi, N. Choudhary, G. H. Han, J. Park, D. Akinwande, and Y. H. Lee, Mater. Today **20**, 116 (2017).

[3] Q. H. Wang, K. Kalantar-Zadeh, A. Kis, J. N. Coleman, and M. S. Strano, Nat. Nanotechnol. **7**, 699 (2012).

[4] K. F. Mak, C. Lee, J. Hone, J. Shan, and T. F. Heinz, Phys. Rev. Lett. **105**, 136805 (2010).

[5] B. Radisavljevic, A. Radenovic, J. Brivio, V. Giacometti, and A. Kis, Nat. Nanotechnol. **6**, 147 (2011).

[6] A. Splendiani, L. Sun, Y. Zhang, T. Li, J. Kim, C. Y. Chim, G. Galli, and F. Wang, Nano Lett. **10**, 1271 (2010).

[7] M. Bernardi, M. Palummo, and J. C. Grossman, Nano Lett. **13**, 3664 (2013).

[8] Y. Yoon, K. Ganapathi, and S. Salahuddin, Nano Lett. **11**, 3768 (2011).

[9] R. Lv, J. A. Robinson, R. E. Schaak, D. Sun, Y. Sun, T. E. Mallouk, and M. Terrones, Acc. Chem. Res. **48**, 56 (2015).

[10] W. S. Yun, S. W. Han, S. C. Hong, I. G. Kim, and J. D. Lee, Phys. Rev. B **85**, 033305 (2012).

[11] G. R. Bhimanapati, Z. Lin, V. Meunier, Y. Jung, J. Cha, S. Das, D. Xiao, Y. Son, M. S. Strano, V. R. Cooper, L. Liang, S. G. Louie, E. Ringe, W. Zhou, S. S. Kim, R. R. Naik, B. G. Sumpter, H. Terrones, F. Xia, Y. Wang, J. Zhu, D. Akinwande, N. Alem, J. A. Schuller, R. E. Schaak, M. Terrones, and J. A. Robinson, ACS Nano **9**, 11509 (2015).

[12] Y. Zhao, J. Qiao, P. Yu, Z. Hu, Z. Lin, S. P. Lau, Z. Liu, W. Ji, and Y. Chai, Adv. Mater. **28**, 2399 (2016).

[13] J. Sun, H. Shi, T. Siegrist, and D. J. Singh, Appl. Phys. Lett. **107**, 153902 (2015).

[14] Y. Wang, Y. Li, and Z. Chen, J. Mater. Chem. C **3**, 9603 (2015).

[15] A. D. Oyedele, S. Yang, L. Liang, A. A. Puretzky, K. Wang, J. Zhang, P. Yu, P. R. Pudasaini, A. W. Ghosh, Z. Liu, C. M. Rouleau, B. G. Sumpter, M. F. Chisholm, W. Zhou, P. D. Rack, D. B. Geohegan, and K. Xiao, J. Am. Chem. Soc. **139**, 14090 (2017).

[16] J. Lin, S. Zuluaga, P. Yu, Z. Liu, S. T. Pantelides, and K. Suenaga, Phys. Rev. Lett. **119**, 016101 (2017).

[17] W. L. Chow, P. Yu, F. Liu, J. Hong, X. Wang, Q. Zeng, C.-H. Hsu, C. Zhu, J. Zhou, X. Wang, J. Xia, J. Yan, Y. Chen, D. Wu, T. Yu, Z. Shen, H. Lin, C. Jin, B. K. Tay, and Z. Liu, Adv. Mater. **29**, 1602969 (2017).

[18] D. Qin, P. Yan, G. Ding, X. Ge, H. Song, and G. Gao, Sci. Rep. **8**, 2764 (2018).

[19] X. Zhang, Z. Zhang, D. Wu, X. Zhang, X. Zhao, and Z. Zhou, Small Methods **2**, 1700359 (2018).

[20] E. Li, D. Wang, P. Fan, R. Zhang, Y. Y. Zhang, G. Li, J. Mao, Y. Wang, X. Lin, S. Du, and H. J. Gao, Nano Res. **11**, 5858 (2018).

[21] M. M. Ugeda, A. J. Bradley, S. F. Shi, F. H. Da Jornada, Y. Zhang, D. Y. Qiu, W. Ruan, S. K. Mo, Z. Hussain, Z. X. Shen, F. Wang, S. G. Louie, and M. F. Crommie, Nat. Mater. **13**, 1091 (2014).

[22] A. V. Krasheninnikov, Nat. Mater. **17**, 757 (2018).

[23] M. Bougouma, A. Batan, B. Guel, T. Segato, J. B. Legma, F. Reniers, M.-P. Delplancke-Ogletree, C. Buess-Herman, and T. Doneux, J. Cryst. Growth **363**, 122 (2013).

[24] H.-P. Komsa, J. Kotakoski, S. Kurasch, O. Lehtinen, U. Kaiser, and A. V. Krasheninnikov, Phys. Rev. Lett. **109**, 035503 (2012).

[25] Y. Ma, Y. Dai, M. Guo, C. Niu, J. Lu, and B. Huang, Phys. Chem. Chem. Phys. **13**, 15546 (2011).

[26] W. Zhou, X. Zou, S. Najmaei, Z. Liu, Y. Shi, J. Kong, J. Lou, P. M. Ajayan, B. I. Yakobson, and J.-C. Idrobo, Nano Lett. **13**, 2615 (2013).

[27] S. Zhang, C.-G. Wang, M.-Y. Li, D. Huang, L.-J. Li, W. Ji, and S. Wu, Phys. Rev. Lett. **119**, 046101 (2017).

[28] P. Vancsó, G. Z. Magda, J. Pető, J.-Y. Noh, Y.-S. Kim, C. Hwang, L. P. Biró, and L. Tapasztó, Sci. Rep. **6**, 29726 (2016).

[29] X. Liu, I. Balla, H. Bergeron, and M. C. Hersam, J. Phys. Chem. C **120**, 20798 (2016).

[30] S. Barja, S. Refaely-Abramson, B. Schuler, D. Y. Qiu, A. Pulkin, S. Wickenburg, H. Ryu, M. M. Ugeda, C. Kastl, C. Chen, C. Hwang, A. Schwartzberg, S. Aloni, S.-K. Mo, D. F. Ogletree, M. F. Crommie, O. V. Yazyev, S. G. Louie, J. B. Neaton, and A. Weber-Bargioni, arXiv:1810.03364 (2018).

[31] J. Pető, T. Ollár, P. Vancsó, Z. I. Popov, G. Z. Magda, G. Dobrik, C. Hwang, P. B. Sorokin, and L. Tapasztó, Nat. Chem. **10**, 1246 (2018).

[32] H. Shi, H. Pan, Y.-W. Zhang, and B. I. Yakobson, Phys. Rev. B **87**, 155304 (2013).

[33] D. Y. Qiu, F. H. da Jornada, and S. G. Louie, Phys. Rev. Lett. **111**, 216805 (2013).

[34] A. Ramasubramaniam, Phys. Rev. B **86**, 115409 (2012).

[35] L. Hedin, Phys. Rev. **139**, A796 (1965).

[36] M. S. Hybertsen and S. G. Louie, Phys. Rev. B **34**, 5390 (1986).

[37] L. X. Benedict, E. L. Shirley, and R. B. Bohn, Phys. Rev. Lett. **80**, 4514 (1998).

[38] S. Albrecht, L. Reining, R. Del Sole, and G. Onida, Phys. Rev. Lett. **80**, 4510 (1998).

[39] M. Rohlfing and S. G. Louie, Phys. Rev. Lett. **81**, 2312 (1998).

[40] J. Heyd, G. E. Scuseria, and M. Ernzerhof, J. Chem. Phys. **118**, 8207 (2003).

[41] G. Kresse and J. Furthmüller, Phys. Rev. B **54**, 11169 (1996).

[42] G. Kresse and J. Hafner, Phys. Rev. B **47**, 558 (1993).

[43] P. E. Blöchl, Phys. Rev. B **50**, 17953 (1994).

[44] J. Klimeš, D. R. Bowler, and A. Michaelides, Phys. Rev. B **83**, 195131 (2011).

[45] A. A. Mostofi, J. R. Yates, Y.-S. Lee, I. Souza, D. Vanderbilt, and N. Marzari, Comput. Phys. Commun. **178**, 685 (2008).

[46] H. J. Monkhorst and J. D. Pack, Phys. Rev. B **13**, 5188 (1976).

[47] L. Jelver, P. M. Larsen, D. Stradi, K. Stokbro, and K. W. Jacobsen, Phys. Rev. B **96**, 085306 (2017).

[48] D. Stradi, L. Jelver, S. Smidstrup, and K. Stokbro, J. Phys. Condens. Matter **29**, 185901 (2017).

[49] K. Momma and F. Izumi, J. Appl. Crystallogr. **44**, 1272 (2011).

[50] C. Soulard, X. Rocquefelte, P.-E. Petit, M. Evain, S. Jobic, J.-P. Itié, P. Munsch, H.-J. Koo, and M.-H. Whangbo, Inorg. Chem. **43**, 1943 (2004).

[51] M. E. J.P. Perdew, K. Burke, Phys. Rev. Lett. **77**, 3865 (1996).

[52] S. Grimme, J. Comput. Chem. **27**, 1787 (2006).

[53] S. Grimme, J. Antony, S. Ehrlich, and H. Krieg, J. Chem. Phys. **132**, 154104 (2010).

[54] F. Grønvold and E. Røst, Acta Crystallogr. **10**, 329 (1957).

[55] S.-H. Zhang and B.-G. Liu, J. Mater. Chem. C **6**, 6792 (2018).

[56] C. Long, Y. Liang, H. Jin, B. Huang, and Y. Dai, ACS Appl. Energy Mater. **2**, 513 (2018).

[57] X. Zhu, F. Li, Y. Wang, M. Qiao, and Y. Li, J. Mater. Chem. C **6**, 4494 (2018).

[58] M. Shishkin and G. Kresse, Phys. Rev. B - Condens. Matter Mater. Phys. **75**, 235102 (2007).

[59] J. S. Ross, P. Rivera, J. Schaibley, E. Lee-Wong, H. Yu, T. Taniguchi, K. Watanabe, J. Yan, D. Mandrus, D. Cobden, W. Yao, and X. Xu, Nano Lett. **17**, 638 (2017).

[60] P. Rivera, H. Yu, K. L. Seyler, N. P. Wilson, W. Yao, and X. Xu, Nat. Nanotechnol. **13**, 1004 (2018).

[61] L.-H. Zeng, D. Wu, S.-H. Lin, C. Xie, H.-Y. Yuan, W. Lu, S. P. Lau, Y. Chai, L.-B. Luo, Z.-J. Li, and Y. H. Tsang, Adv. Funct. Mater. **29**, 1806878 (2019).